Density functional theory-assisted 31P and 23Na magic-angle spinning nuclear magnetic resonance study of the Na3V2(PO4)2F3–Na3V2(PO4)2FO2 solid solution: unraveling Its local and electronic structures

Long H. B. Nguyen, Paula Sanz Camacho, Thibault Broux, Jacob Olchowka, Christian Masquelier, Laurence Croguennec, Dany Carlier-Larregaray

DFT-assisted ^{31}P and ^{23}Na MAS-NMR Study of the $Na_3V_2(PO_4)_2F_3$ – $Na_3V_2(PO_4)_2FO_2$ Solid Solution: Unravelling its Local and Electronic Structures

Long H. B. Nguyen [a,b,c], *Paula Sanz Camacho* [a,c], *Thibault Broux* [a,b,c,d], *Jacob Olchowka* [a,c,d], *Christian Masquelier* [b,c,d], *Laurence Croguennec* [a,c,d], *and Dany Carlier* [a,c,d] *

[a] CNRS, Univ. Bordeaux, Bordeaux INP, ICMCB UMR CNRS #5026, F-33600, Pessac, France.

[b] Laboratoire de Réactivité et de Chimie des Solides, Université de Picardie Jules Verne, UMR CNRS #7314, 80039 Amiens Cedex 1, France.

[c] RS2E, Réseau Français sur le Stockage Electrochimique de l'Energie, FR CNRS #3459, F-80039 Amiens Cedex 1, France.

[d] ALISTORE-ERI European Research Institute, FR CNRS #3104, Amiens, F-80039 Cedex 1, France.

Key words: $Na_3V_2(PO_4)_2F_3$, $Na_3V_2(PO_4)_2FO_2$, solid-state NMR, Fermi contact, electron spin transfer, first-principles DFT calculations, structural distortion.

* Corresponding author: D. Carlier (Dany.Carlier@icmcb.cnrs.fr)

Abstract

The local and electronic structures of the $Na_3V_2(PO_4)_2F_3$ – $Na_3V_2(PO_4)_2FO_2$ electrode materials have been investigated by a combination of ^{23}Na and ^{31}P magic-angle spinning NMR spectroscopy and Density Functional Theory calculations. The spins distribution and the ^{31}P NMR Fermi contact shifts in these materials were calculated based on the projector augmented wave approach implemented in the VASP code. Upon oxygen substitution, some V^{4+} ions are formed and involved in highly covalent vanadyl bond. We show that they exhibit a very specific electronic structure with a single electron on the $3d_{xy}$ orbital perpendicular to the bi-octahedra axis. The V^{3+} ions, on the other end, exhibit a partial occupation of the t_{2g} orbitals by two electrons. The peculiar electronic structure of the V ions is at the origin of the complex spin transfer mechanisms observed in the $Na_3V_2(PO_4)_2F_3$ – $Na_3V_2(PO_4)_2FO_2$ materials and results in the existence of several ^{23}Na and ^{31}P MAS NMR resonances. We also demonstrate here that a ^{31}P MAS NMR signal close to 0 ppm can also be observed in paramagnetic materials if there is no proper orbital overlap for the electron spin transfer to occur. Thanks to the proper signal assignment achieved using DFT calculations, we could estimate the degree of substitution of oxygen for fluorine in the materials and discuss the local distribution of V^{3+}/V^{4+} ions.

▪ INTRODUCTION

Over the last few decades, rechargeable lithium-ion batteries (LIBs) have been one of the most dominant means of energy storage for portable devices due to their high operating voltage and high energy density.[1,2] Nevertheless, the unequal distribution of lithium resources and its high price have led to a call on the development of alternative systems which can be used in parallel to LIBs.[3] Among the prototypes that have been recently developed, sodium-ion batteries (SIBs) are the most promising ones.[4] In most of the cases, the active materials used in positive electrodes in LIBs and SIBs contain transition metal ions possessing one or several unpaired electron(s). The presence of these unpaired electrons usually modifies significantly the magnetic field surrounding the nuclei in the crystal structure and results in highly shifted resonant frequencies on the recorded nuclear magnetic resonance (NMR) spectra of the nucleus of interest. The interpretation of NMR resonances of paramagnetic materials is often challenging and requires the help from density functional theory (DFT) calculations. Nevertheless, the use of paramagnetic NMR spectroscopy has been increasing significantly in recent years and is applied widely in the field of batteries. An insightful analysis of paramagnetic NMR spectra can provide important information on the atomic local environment as well as the electronic structure of the observed nuclei, such as the coordination number, the oxidation state and the number of unpaired electrons of the transitional metal ions which are adjacent to it.[5]

$^{6/7}$Li, ^{23}Na, and ^{31}P are the three most common NMR active nuclei encountered in the field of batteries. $^{6/7}$Li, ^{23}Na, and ^{31}P solid-state NMR (*ss*-NMR) spectroscopies were used extensively to study local environments in $LiCoO_2$-related materials, $LiMn_2O_4$, $LiFePO_4$, and Na_2FePO_4F.[6–12] Furthermore, ^{7}Li and ^{23}Na *ss*-NMR were used as key tools to probe the layer shearing process in P2-$Na_x[Li_yNi_zMn_{1-y-z}]O_2$ ($x,y,z \leq 1$) materials.[13] Thanks to its high sensitivity

to the atomic local environment, *ss*-NMR was also used to detect atomic defects that can exist in various crystal structures: $Na_3V_2(PO_4)_2F_3$ has long been reported to be a pure phase containing only V^{3+}; however, by the use of ^{31}P *ss*-NMR our group has recently explained the origin of the structural and electrochemical discrepancies reported in literature for $Na_3V_2(PO_4)_2F_3$. Indeed, most of $Na_3V_2(PO_4)_2F_3$ phases reported in the literature appeared to be slightly oxidized by the partial substitution of oxygen for fluorine leading to the formation of $Na_3V_2(PO_4)_2F_{3-\delta}O_\delta$ ($\delta \sim 0$) with highly covalent vanadyl-type bonds (V^{4+}=O).[14] The use of ^7Li *ss*-NMR to detect the formation of oxygen defects in $LiVPO_4F_{1-y}O_y$ ($0 \leq y \leq 1$) phases was also highlighted in our recent studies.[15–17] Although with weaker spectral resolution, *Operando* NMR technique has also been developed to investigate processes occurring in batteries upon cycling.[18–23]

For paramagnetic materials, the observed resonances are usually broad and highly shifted due to the electron-nuclear spin interaction, which is also known as the hyperfine shift.[5] The hyperfine shift can occur (*i*) through space by the electron-nuclear dipolar coupling, which broadens the line shape of the observed resonances and can be partially suppressed using Magic Angle Spinning (MAS), and (*ii*) through chemical bonds (Fermi contact), which results in a highly shifted resonant value.[5,24] The Fermi contact can further be classified into spin delocalization and spin polarization mechanisms. The former contact leads to a positive Fermi contact shift while the latter induces a negative value. A schematic description of the spin delocalization and spin polarization mechanisms in transition metal oxides was reported by some of us,[24] which could also be used to predict the sign of the observed resonances in similar structures. In paramagnetic polyanionic materials, the spin transfer can still occur through the Fermi contact, however the spin interaction pathways are usually not obvious and it is difficult to make a general formalism due to the variety of the polyanionic frameworks.

$Na_3V_2(PO_4)_2F_3$ was recently reported to be a prospective positive electrode material for SIBs as a result of its high operating voltage, high energy density, excellent cycling stability and remarkable rate capability.[25–28] One of the first ^{31}P *ss*-NMR measurements on $Na_3V_2(PO_4)_2F_3$ was reported by Liu *et al*.[29] The recorded spectrum revealed the presence of two resonances at 6000 ppm and 4500 ppm, which were then assigned to the non-equivalent crystallographic P(1) and P(2) sites of the crystal structure described in the $P4_2/mnm$ space group. Recently, some of us revisited the crystal structure of $Na_3V_2(PO_4)_2F_3$ and discovered that the structure should rather be described in the *Amam* space group with a single phosphorus site.[30] Park *et al*. discovered that the terminal fluorine atoms in $Na_3V_2(PO_4)_2F_3$ can easily be replaced by oxygen leading to the formation of a family of materials with the general formula $Na_3V^{3+}_{2-y'}V^{4+}_{y'}(PO_4)_2F_{3-y'}O_{y'}$ ($0 \leq y' \leq 2$), where $Na_3V_2(PO_4)_2F_3$ and $Na_3V_2(PO_4)_2FO_2$ are the two end members of this solid solution. The partial oxygen substitution for fluorine leads to the oxidation of some V^{3+} to V^{4+} ions and to the formation of very covalent vanadyl-type bonds. The crystal structure of this family of materials was indexed in the $P4_2/mnm$ space group.[26] Our group has recently revisited the crystal structure of these compositions by the use of high resolution synchrotron X-ray powder diffraction (SXRPD) and showed that *Amam* was in fact the most appropriate space group that should be used to describe their structure, except for $Na_3V_2(PO_4)_2FO_2$ where a modulated vector in the $P2_1/m$ space group is required to take into account the Na^+-vacancy ordering in the structure.[14,31] The ^{31}P *ss*-NMR spectra of several members of the $Na_3V_2(PO_4)_2F_3$ – $Na_3V_2(PO_4)_2FO_2$ family were also reported and revealed a more complicated scenario with five resonances at 6000 ppm, 4500 ppm, 3000 ppm, 1500 ppm, and 0 ppm in all the intermediate phases of this solid solution.[14]

In this paper, we first aim to confirm the ^{23}Na and ^{31}P NMR signal assignments proposed previously for the $Na_3V^{3+}_{2-y'}V^{4+}_{y'}(PO_4)_2F_{3-y'}O_{y'}$ ($0 \leq y' \leq 2$) material series,[14] using DFT calculations. Then, we will focus on investigating the occurring spin transfer mechanisms by a

combination of DFT calculations and the concept of orbital overlap, hoping this will lead to a better understanding of both local atomic and electronic structures of these materials. Finally, as a local probe and with a proper signal assignment, the NMR results allow a discussion on the V^{3+}/V^{4+} ionic repartition in the lattice.

▪ METHODS

Material Preparations. The oxygen-substituted $Na_3V^{3+}_{2-y'}V^{4+}_{y'}(PO_4)_2F_{3-y'}O_{y'}$ ($0 \leq y' \leq 2$) materials were obtained by following the solid-state synthesis route described in details elsewhere.[14,26] The as-obtained materials were washed in distilled water at ambient temperature during four nights to eliminate impurities traces. Their in-depth structural and electrochemical characterizations are reported in [14,26]. Some of us had earlier reported the ^{23}Na and ^{31}P *ss*-NMR characterization of the $Na_3V^{3+}_{2-y}V^{4+}_{y}(PO_4)_2F_{3-y}O_y$ phases for $0 \leq y \leq 0.5$ [14]; however, we have recently found out that the degree of oxygen substitution in these phases was in fact two times more extended than reported [31] and the proper chemical formula of all the compositions reported in [14] should be re-written as $Na_3V^{3+}_{2-y'}V^{4+}_{y'}(PO_4)_2F_{3-y'}O_{y'}$ ($0 \leq y' \leq 1.0$ and $y' = 2y$) with y being the value of oxygen-substitution reported in [14]. The synchrotron X-ray diffraction patterns of all the synthesized $Na_3V^{3+}_{2-y'}V^{4+}_{y'}(PO_4)_2F_{3-y'}O_{y'}$ ($0 \leq y' \leq 2.0$) compositions are given in **Figure S1**. An Al-substituted phase, $Na_3V_{1.5}Al_{0.5}(PO_4)_2F_3$, was obtained by a sol-gel synthesis method as reported in [32].

Solid-State Nuclear Magnetic Resonance Measurement. ^{31}P *ss*-NMR spectra were acquired on a Bruker Avance III spectrometer with a 2.35T magnetic field at a resonance frequency of 40.6 MHz by using a standard Bruker 2.5 mm magic-angle spinning (MAS) probe with a 30 kHz spinning frequency. A Hann echo sequence was applied with a 90^o pulse 1.1 μs

and a recycle delay of 1 s. H_3PO_4 85% (Sigma-Aldrich) was used as external reference for 0 ppm chemical shift.

^{23}Na *ss*-NMR spectra were acquired using a Bruker Avance 500 MHz spectrometer, equipped with a 11.7 T widebore magnet (operating at the Larmor frequency of 132.3 MHz for ^{23}Na). Experiments were performed using a conventional 2.5 mm MAS probe, with 30 kHz MAS rate. Chemical shifts are referenced relative to an aqueous 0.1M NaCl solution at 0 ppm. In each case, a short pulse length of 1.1 μs corresponding to a selective $\pi/8$ pulse determined by using a 0.1 M NaCl aqueous solution was employed. The spectral width was set to 1 MHz and the recycle delay of 0.5 s, which was long enough to avoid T_1 saturation effects. The baseline distortions resulted from the spectrometer dead time (5-10 μs) were removed computationally by using a polynomial baseline correction routine. The obtained data was processed by TopSpin and DM-fit softwares.[33]

Density Functional Theory Calculations. First-principles calculations were performed within the DFT framework, and the calculations using the projector augmented wave (PAW) method were computed with the Vienna *ab initio* simulation package (VASP) code.[34] A wave plane cutoff energy of 600 eV and a *k*-mesh of 2x2x2 were applied. The experimental crystal structure of the materials was used as the input model and the calculations were spin polarized type with ferromagnetic ordering, which is appropriate to take into account the Fermi contact interaction as discussed in [24]. The energy minimization and electron density on each atom were calculated by using the generalized gradient approximation (GGA) and GGA+U approaches, where the Hubbard type interaction is added to the latter method to localize *d* electrons. In this study, the U values of 3.0, 4.0, and 5.0 eV were tested.

The isotropic shift of a specific nucleus due to Fermi contact can then be quantified from the electron spin density:

$$\delta_{iso}^{i} = \frac{1}{3SN_A}\,\rho^{i}(0)\chi_M(T) \qquad (3)$$

where S is the spin quantum number of the paramagnetic ion, $\rho^{i}(0)$ is the computed spin density on the *i* nucleus as given in ref. [15], and $\chi_M(T)$ is the molar magnetic susceptibility at the temperature where the NMR spectrum was recorded. The temperature (*T*) was chosen to be 320K, which is the approximate temperature inside the rotor at a spinning rate of 30 *k*Hz.

The following nuclear gyromagnetic ratio ($MHz \cdot T^{-1}$) were used for the calculations: 11.215 (^{51}V), 17.2538 (^{31}P), 11.271 (^{23}Na), 40.078 (^{19}F), and 5.775 (^{17}O). The Curie temperature was assumed to be 0K for all compounds and the theoretical value of molar magnetic susceptibility calculated by Curie law was used for the Fermi contact shift calculations.

The partial density of states on vanadium ions were calculated by considering the ionic radius of V^{3+} equals to 0.55 Å.[35] The 3D charge density and electronic spin density distribution maps were visualized utilizing VESTA software.[36]

▪ RESULTS AND DISCUSSIONS

^{31}P *ss*-NMR Measurements in the $Na_3V_2(PO_4)_2F_3$ - $Na_3V_2(PO_4)_2FO_2$ solid solution

Figure 1 shows the ^{31}P *ss*-NMR spectra already reported in [14] for the $Na_3V^{3+}_{2-y'}V^{4+}_{y'}(PO_4)_2F_{3-y'}O_{y'}$ compositions in the range of $0 < y' \leq 1$, and a comparison with those recently recorded for the more oxidized phases $Na_3V_2(PO_4)_2F_{1.5}O_{1.5}$ ($y' = 1.5$) and $Na_3V_2(PO_4)_2FO_2$ ($y' = 2$). This set of spectra allows us to get an insight into the origin of the ^{31}P *ss*-NMR spectra of the whole composition range. For $Na_3V_2(PO_4)_2F_3$ ($y' = 0$), the main ^{31}P resonance was observed at ~ 6000 ppm and was assigned to the $P(OV^{3+})_4$ unit as the dominant

phosphorus local environment. In addition to the main signal, a second resonance around 4500 ppm was also detected due to the presence of oxygen defects in the structure leading to the formation of the $P(OV^{3+})_3(OV^{4+})$ local environment.[14] In the $Na_3V^{3+}_{2-y'}V^{4+}_{y'}(PO_4)_2F_{3-y'}O_{y'}$ ($0 < y' < 1$) series, in addition to the 6000 ppm signal, four new resonances were observed at 4500 ppm, 3000 ppm, 1500 ppm and ~ 0 ppm, whose intensity varied as a function of the O-content. We had earlier speculated that these signals could be originated from different phosphorus local environments in the structure by considering the first vanadium coordination sphere: $P(OV^{3+})_3(OV^{4+})$, $P(OV^{3+})_2(OV^{4+})_2$, $P(OV^{3+})(OV^{4+})_3$, and $P(OV^{4+})_4$, respectively.[14] The broadening and the asymmetry of some signals can be resulted from various ^{31}P environments if one considers also the second vanadium coordination sphere, *i.e.* the second vanadium site of a given bi-octahedron. Among those signals, it was really surprising to observe a very narrow signal at ~ 0 ppm corresponding to the $P(OV^{4+})_4$ local environment, as V^{4+} ions are paramagnetic.

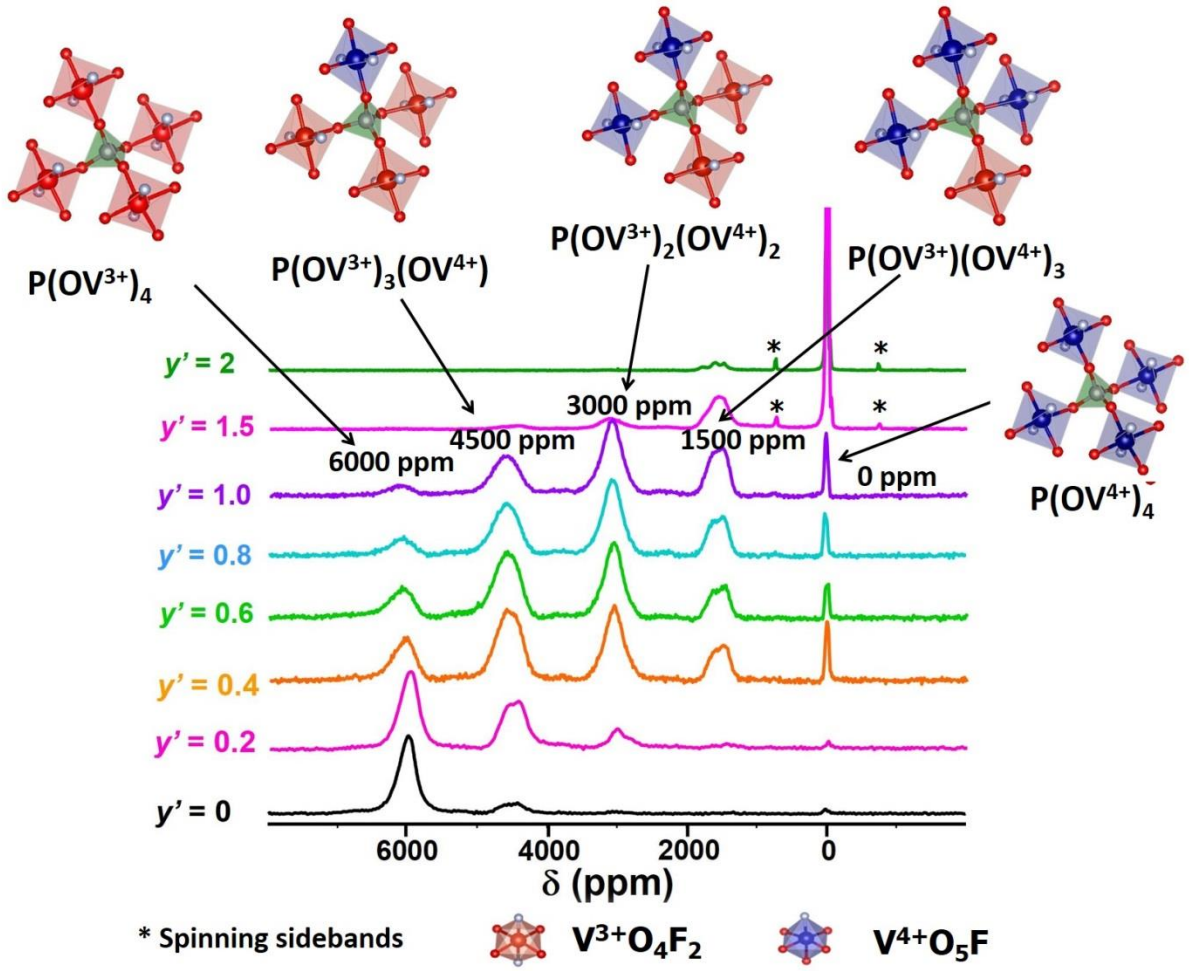

Figure 1: *Hahn echo ^{31}P MAS NMR spectra of the $Na_3V^{3+}_{2-y'}V^{4+}_{y'}(PO_4)_2F_{3-y'}O_{y'}$ ($0 \leq y' \leq 2$) samples (B_0= 2.35T; ν_R= 30 kHz). The spinning sidebands are marked with asterisks. The PO_4 tetrahedral units are in green while the $V^{3+}O_4F_2$ and $V^{4+}O_5F_1$ octahedral units are in red and blue, respectively.*

In fact, for the $Na_3V_2(PO_4)_2FO_2$ (y' = 2) composition, where $P(OV^{4+})_4$ is the only permitted phosphorus environment, the main and highly intense resonance is recorded nearby 0 ppm (**Figure 1**). This latest finding thus confirms the hypothesis that some of us had proposed earlier in [14], and proves that there is no electron-nuclear spin interaction between the unpaired electron of V^{4+} and phosphorus nuclei in the $P(OV^{4+})_4$ local environment in this structural framework, which gives rise to a ^{31}P NMR shift value in the diamagnetic region. First-principles calculations were performed on $Na_3V^{3+}_2(PO_4)_2F_3$, $Na_3V^{4+}_2(PO_4)_2FO_2$, and $Na_3V^{3+}V^{4+}(PO_4)_2F_2O$ in order to understand the electronic structure of the existing vanadium

ions as well as the mechanism of the spin interaction between the unpaired electron(s) of V^{3+}/V^{4+} and the phosphorus nuclei in these structures.

Local electronic structure around the vanadium ions in $Na_3V_2(PO_4)_2F_3$ and in $Na_3V_2(PO_4)_2FO_2$

In order to perform DFT calculations, we aimed at using the experimental crystal structure of $Na_3V_2(PO_4)_2F_3$ as input model. However, it contains three different Na crystallographic sites, Na1, Na2, and Na3, in which Na1 is fully occupied whereas the other two have partial occupancies (**Figure S2**).[30] An approximate model structure had thus to be considered in our DFT calculations. Considering the close proximity (0.90 Å) between the two partially occupied Na2 and Na3 sites, an approximate input model was created by placing a fully occupied Na2' site on the barycenter between Na2 and Na3. This input model was then used in the structural relaxation step and the DFT optimized structure is compared to the experimental one in **Figure S2**. Since here we focus on the Fermi contact shift calculations between vanadium ions and ^{31}P nuclei, we do not expect a strong influence of Na positions on the strength of this Fermi contact. The structure was first relaxed using GGA or GGA+U methods. The optimized structure of $Na_3V_2(PO_4)_2F_3$ crystallizes in an orthorhombic system, which is in good agreement with the experimental *Amam* space group (**Table S1**). The optimized cell parameters (*a*, *b*, and *c*) calculated by the GGA method are in the error range of 1% in comparison to those obtained experimentally by diffraction. Using GGA+U (here U = 3 *eV*, 4 *eV*, and 5 *eV*), a greater deviation from the experimental data is observed (**Table S1**) suggesting that the GGA method is a better choice to study this material.

For $Na_3V_2(PO_4)_2FO_2$, the situation is more complex. The crystal structure of $Na_3V_2(PO_4)_2FO_2$ had been studied in details by Tsirlin *et al*. and had been reported to crystallize

in the $P4_2/mnm$ space group, which contained a fully occupied Na1 site and a half occupied Na2 site with a distance of 2.374 Å between the two closest Na2 sites (**Figure S3**).[37] We have recently revisited the crystal structure of this material by high resolution SXRPD [31] and we have in fact shown that the structure is even more complex: it should be described in a monoclinic cell with a vector of modulation q = ½ b* + ½ c* in the $P2_1/m$ space group that takes into account a long-range ordering of Na^+ ions on three different partially occupied sites Na1, Na2 and Na3.[31] As in the case of $Na_3V_2(PO_4)_2F_3$, partially occupied sites cannot be taken into account in DFT calculations, we therefore retained the structural description reported by Tsirlin *et al*. where a fully occupied Na3' site was placed at the barycenter between two Na2 sites despite the great distance between the two actual sites (**Figure S3**). The input model relaxes into a tetragonal cell whose unit cell parameters are in agreement with those reported by Tsirlin *et al*.[37] As for $Na_3V_2(PO_4)_2F_3$, upon increasing the U values, the cell parameters deviate from the experimental ones (**Table S2**).

The optimized V–O, V–F distances and the density of states (DOS) calculation of vanadium ions in $Na_3V_2(PO_4)_2F_3$ both agree with the presence of V^{3+} ion a symmetric octahedral site formed by four oxygen atoms in the basal plane of the octahedron and two fluorine atoms on the axial positions, one of which being shared with the neighboring V^{3+} site (**Figure 2a**), as reported experimentally.[30,38] The difference between the experimental and the calculated V–O, V–F, and P–O distances is less than 1% with GGA (**Figure 2a**). Despite the difference in the nature of fluorine and oxygen, the V^{3+} site is 'quasi'-symmetric as the six surrounding bond lengths are nearly similar (~ 2.0 Å) (**Figure 2a**).

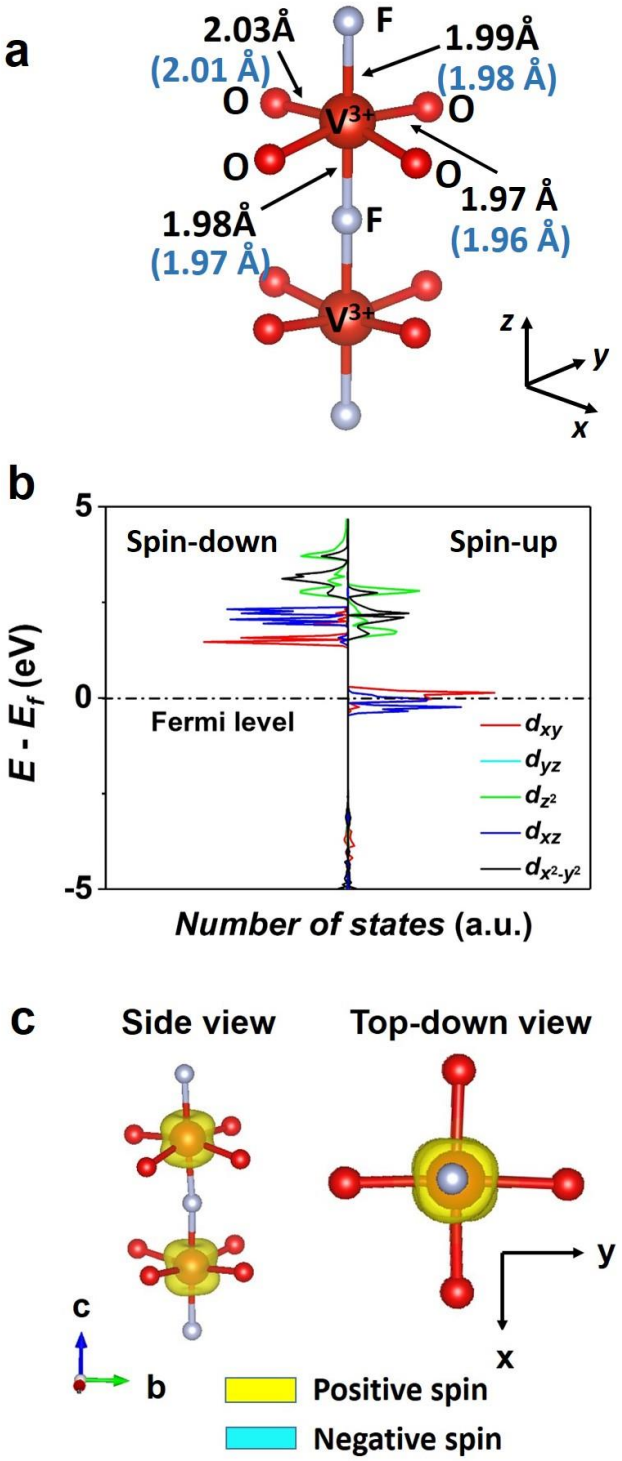

Figure 2: *(a) Local environment of V^{3+} in $Na_3V_2(PO_4)_2F_3$, with the optimized distances compared to the experimental ones given in parentheses ; (b) Calculated partial DOS around the vanadium ions in $Na_3V_2(PO_4)_2F_3$ using the GGA method; (c) Calculated spin distribution map surrounding a $V_2O_8F_3$ bi-octahedral unit. An iso-surface value of $8{\cdot}10^{-3}$ electron.Å^{-2} was used for this plot. The positive and negative electron spin are represented in yellow and blue, respectively.*

The partial DOS around vanadium ions in $Na_3V_2(PO_4)_2F_3$ indicates that the two unpaired electrons of V^{3+} ions are partially located in the three d_{xy}, d_{xz}, and d_{yz} (t_{2g}) orbitals (**Figure 2b**). The *x*, *y*, and *z* directions used to define the orientation of the orbitals were chosen to run along the 'ligand – V^{n+}' interatomic axes: *x* and *y* axes running along the V–O bonds in the basal plane while the *z* axis orienting along the bi-octahedron axis, all of them are independent of the *a*, *b*, and *c* crystallographic directions of the unit cell. **Figure 2c** shows the 3D electronic spin distribution map calculated for $Na_3V_2(PO_4)_2F_3$, which allows to visualize the local spin distribution in the t_{2g} orbitals. The two V^{3+} ions in the bi-octahedral units of $Na_3V_2(PO_4)_2F_3$ exhibit similar spin distribution, with a maximum spin concentration in lobes pointing in-between the two V–O bonds in the basal plane or in-between the V–O and V–F bonds in the (*xz*) and (*yz*) planes, thus confirming the partial occupancy of the three t_{2g} orbitals.

For $Na_3V_2(PO_4)_2FO_2$, the vanadium ions reside in octahedral sites formed by four equal V–O bonds (1.97 Å) in the basal plane, a very short V=O bond (1.62 Å), and a long V–F bond (2.1 Å), where the fluorine is shared with another vanadium ion in the axial position (**Figure 3a**). The calculated partial DOS on V shows that vanadium ions are in the +4 oxidation state, as expected, and that the single unpaired electron is located only in the d_{xy} orbital which is perpendicular to the bi-octahedron axis (**Figure 3b**). Due to the presence of a short vanadyl bond, a distortion occurs on all VO_5F sites, lowering the O_h symmetry to C_{4v} locally. As a consequence, the t_{2g} orbitals of V^{4+} are split into b_2 (d_{xy}) and e (d_{xz}, d_{yz}) sub-groups while e_g orbitals will be split further into b_2 ($d_{x^2-y^2}$) and a_1 (d_{z^2}). The splitting scheme and the relative energy of the orbitals in this case are shown in **Figure S4**. The orbital d_{xy} has therefore the lowest energy value and is occupied by the single electron of V^{4+}, with the δ_2 splitting energy of 0.426 *eV* being higher than kT at ambient temperature (25 meV) (**Figure 3b**).The 3D spin density map plotted for a bi-octahedron in $Na_3V_2(PO_4)_2FO_2$ confirms the localization of the

spin density only in lobes pointing in-between two V–O bonds in the basal plane, which is perpendicular to the bi-octahedron axis (**Figure 3c**).

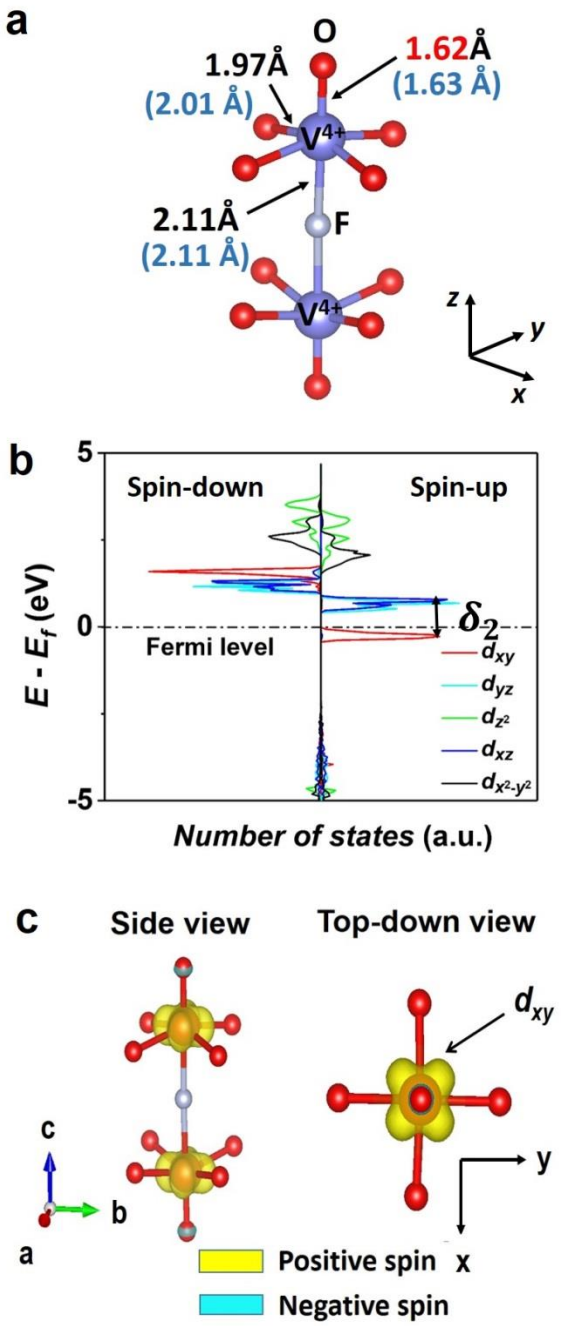

***Figure 3** : (a) Local environment of V^{4+} in $Na_3V_2(PO_4)_2FO_2$ with the optimized distances compared to the experimental ones given in parentheses; (b) DOS diagram of V^{4+} in $Na_3V_2(PO_4)_2FO_2$ calculated by GGA method. Only the 'spin-up' state of d_{xy} orbital is occupied; (c) Calculated spin distribution map surrounding a $V_2O_{10}F$ bi-octahedral unit. An iso-surface value of $2{\cdot}10^{-2}$ electron$\cdot$Å^{-2} was used for this plot. The single electron of V^{4+} occupies the d_{xy} orbital uniquely. The positive and negative electron spin are represented in yellow and blue, respectively.*

Our DFT calculations also provide approximate values of electron spin densities on the nuclei in the structures, thus allowing to compute the expected Fermi contact shifts for ^{31}P and ^{23}Na nuclei by using equations (1), (2) and (3) given in the experimental part.

Table 1 : Calculated ^{31}P Fermi contact NMR shifts (in ppm) in $Na_3V_2(PO_4)_2F_3$ and $Na_3V_2(PO_4)_2FO_2$ using GGA and GGA+U methods, compared to the experimental ones.

	Experimental data	**GGA**	**GGA+3*eV***	**GGA+4*eV***	**GGA+5*eV***
$Na_3V_2(PO_4)_2F_3$					
P1	~ 6000 ppm	6562 ppm	4580 ppm	3943 ppm	3334 ppm
P2		6534 ppm	4598 ppm	3942 ppm	3336 ppm
$Na_3V_2(PO_4)_2FO_2$					
P1	~ 0 ppm	96 ppm	163 ppm	117 ppm	66 ppm
P2		79 ppm	124 ppm	77 ppm	22 ppm

Each unit cell of $Na_3V_2(PO_4)_2F_3$ or $Na_3V_2(PO_4)_2FO_2$ contains two groups of ^{31}P nuclei with different Fermi contact shifts. As seen in **Table 1**, the difference in the calculated shifts for these two groups is however negligible. For $Na_3V_2(PO_4)_2F_3$, the ^{31}P *ss*-NMR Fermi contact shifts computed either by GGA or GGA+U are positive and large, in agreement with the strong interaction expected between V^{3+} ions and P nuclei. As also expected, as the U value increases, the unpaired electrons are more localized on the t_{2g} orbitals of V^{3+} and therefore less delocalized to the neighboring phosphorus nuclei, leading to lower computed shifts.[39] Fermi contact shifts computed within the GGA are in better agreement with the experimental ones. For $Na_3V_2(PO_4)_2FO_2$, whatever the method: GGA or GGA+U, all the calculated ^{31}P *ss*-NMR Fermi contact shifts are very weak and fall in the typical range of shifts for ^{31}P in diamagnetic compounds, which is also in agreement with the experimental observation (**Table 1**). This implies that there should be almost no electron spin transfer from the paramagnetic V^{4+} ions to the phosphorus nuclei. As both the optimized structures and the computed Fermi contact shifts

obtained using the GGA method are in good agreement with the experimental data, and in much better agreement than the GGA+U methods, hence only the GGA results will further be discussed in the following parts.

V^{3+}-O-P / V^{4+}-O-P Spin Transfer Mechanisms

In order to investigate the spin transfer mechanism in $Na_3V_2(PO_4)_2F_3$, 3D electronic spin distribution maps were plotted at different iso-surface values and for different local orientations.

The electron spin transfer occurs through the so-called spin delocalization mechanism, which results from the overlap between the t_{2g} orbitals of the V^{3+} ions (**Figure 4a**) and the p_π orbitals of its neighboring O, which is in turn hybridized with the sp^3 orbitals of P (**Figure 4a**). Among the three partially filled t_{2g} orbitals of V^{3+} ions, it appears that d_{xz} and d_{yz} are the two orbitals mostly involved in the spin transfer, as properly oriented for the π-overlap with O p_π orbital that is also overlapping with sp^3 orbital of P. This results in a d_{xz} (V^{3+}) – p_π (O) – sp^3 (P) hybridization with a 135.8° V–O–P angle as schematized in **Figure 4b**. In $Na_3V_2(PO_4)_2F_3$, each phosphorus is surrounded by four V^{3+} ions and each of them contributes to a Fermi contact shift of around 1500 ppm through the d_{xz}/d_{yz} (V^{3+}) – p_π (O) – sp^3 (P) interaction. In **Figure 4c**, the overall electron spin density map viewed along the *c* direction shows a strong and positive spin density on the P site in this structure, which is the origin of the highly shifted resonance (6000 ppm) observed on the ^{31}P *ss*-NMR.

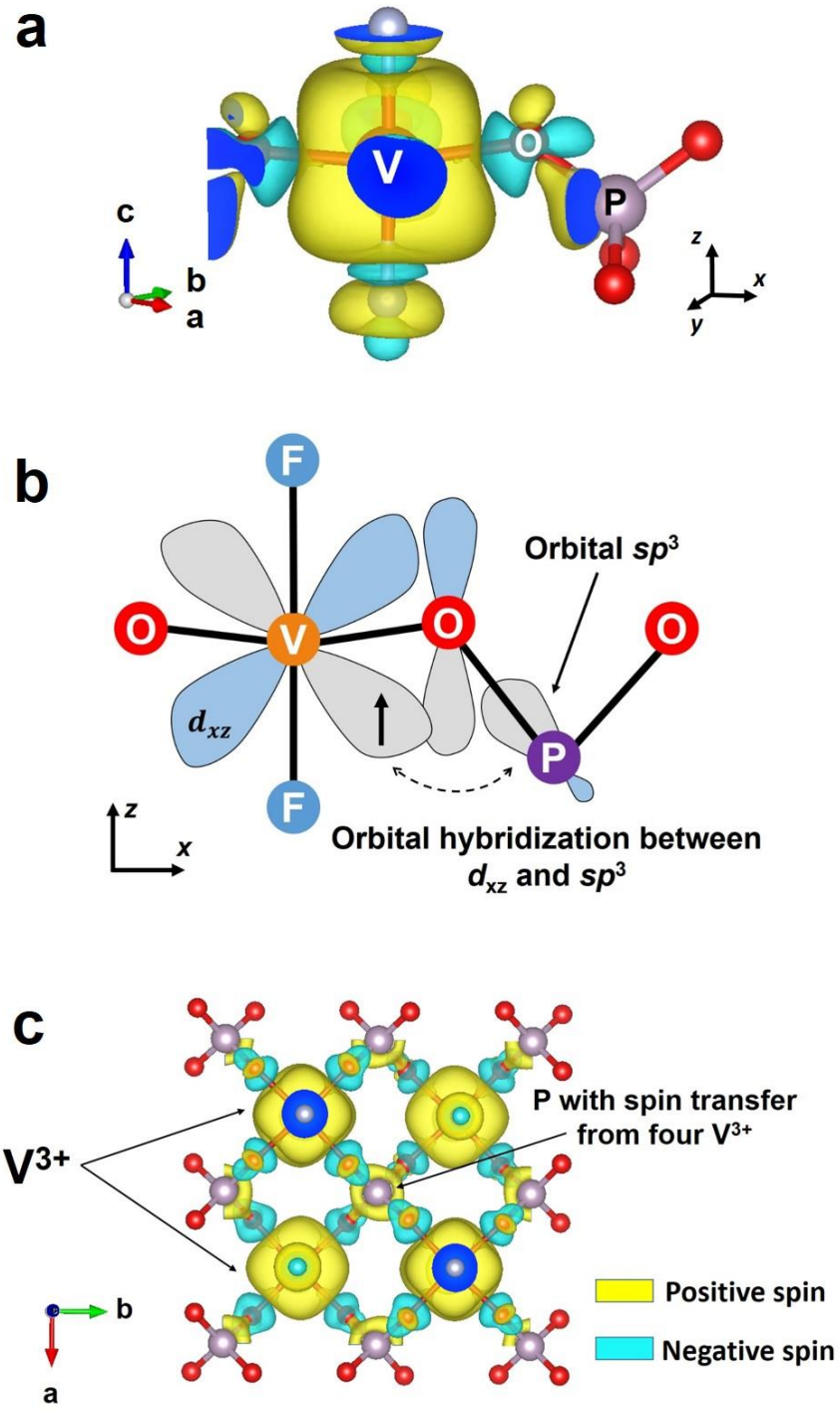

***Figure 4**: (a) 3D calculated spin density map showing the electron spin transfer mechanism from a V^{3+} ion to a neighboring Phosphorus ($8 \cdot 10^{-4}$ electron·Å^{-2} iso-surface value); (b) Schematic representation of the spin transfer mechanism from V^{3+} to P by orbital hybridization model; (c) 3D calculated spin density map ($8 \cdot 10^{-4}$ electron·Å^{-2} iso-surface value) showing that each phosphorus nucleus in $Na_3V_2(PO_4)_2F_3$ receives the electron spin from four neighboring V^{3+} ions. The positive and negative electron spin are represented in yellow and blue, respectively.*

The spin transfer mechanism was also analyzed for $Na_3V_2(PO_4)_2FO_2$. As previously discussed, the two V^{4+} ions of the bi-octahedral units are similar and exhibit one unpaired electron localized only in the d_{xy} orbital perpendicular to the bi-octahedron axis (**Figure 3c** and **Figure 5a**). As seen in **Figure 5b**, no orbital overlap is involving this V^{4+} $3d_{xy}$ orbital and the P sp^3 one. The V^{4+} $3d_{xy}$ orbital is only π-hybridized with one O $2p$ orbital that does not overlap with the P orbitals and the V–O–P angle is equal to 131.9º. However, as can be seen also in **Figure 5b** another O $2p$ orbital, perpendicular to this π-bond, is negatively polarized as there is no overlap with V^{4+} $3d_{xy}$ orbital. One could have actually expected a negative Fermi contact shift for ^{31}P in $Na_3V_2(PO_4)_2FO_2$, but the participation of the P sp^3 orbitals in the negatively deep polarized level should be very weak. This observation explains why we recorded a ^{31}P signal nearby 0 ppm for $Na_3V_2(PO_4)_2FO_2$ despite the presence of paramagnetic V^{4+} ions around P (**Figure 5c**).

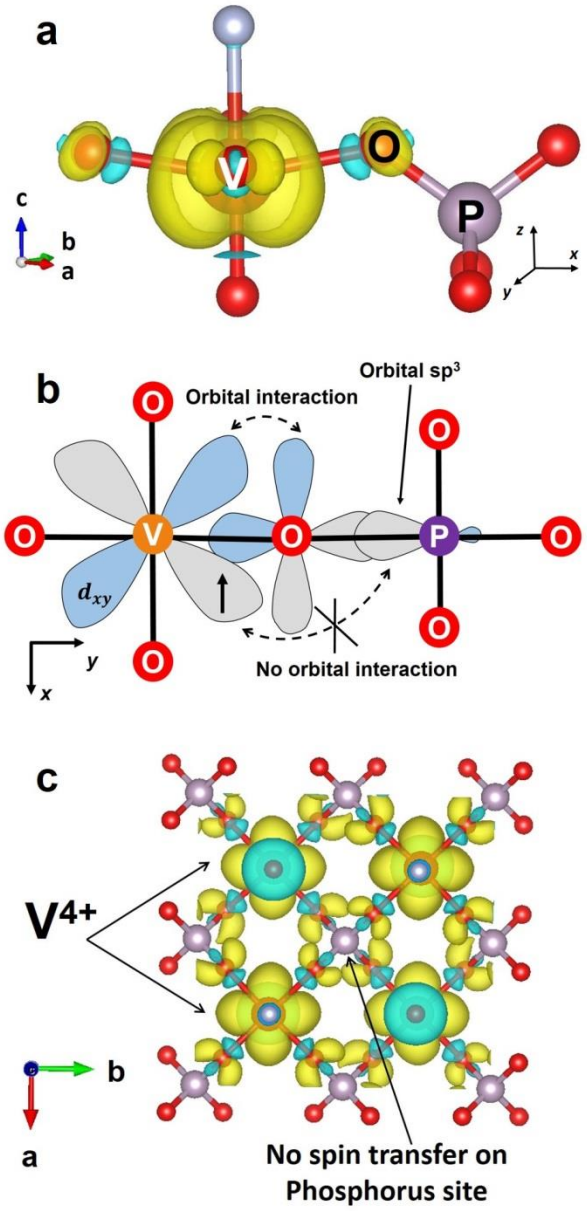

Figure 5 : *(a) 3D calculated spin density map showing the electron spin density surrounding a V^{4+} ion in $Na_3V_2(PO_4)_2FO_2$ ($2{\cdot}10^{-3}$ electron·Å^{-2} iso-surface value); (b) A 2D projection of the V–O–P chemical bond on the (xy) plane of the octahedral unit. The single electron of V^{4+} occupies the d_{xy} orbital, which orients along the diagonal lines of the (xy) plane while the V–O–P bond is formed along the x/y direction; (c) The spin distribution map calculated at $8{\cdot}10^{-4}$ electron·Å^{-2} revealing that there is no spin transfer between V^{4+} ions and phosphorus nuclei in $Na_3V_2(PO_4)_2FO_2$ due to the lack of orbital overlap. The positive and negative electron spin are represented in yellow and blue, respectively.*

We further calculated the spin distribution map for some intermediate compositions in the $Na_3V_2(PO_4)_2F_3$ – $Na_3V_2(PO_4)_2FO_2$ system. In $Na_3V^{3+}V^{4+}(PO_4)_2F_2O$ (y' = 1.0), for example, half of the vanadium ions are expected to be +3 and half +4. The terminal oxygen ions could be distributed differently in the crystal structure leading to different distribution of V^{3+}/V^{4+} ions over the vanadium sites. In order to study the relationship between the V^{3+}/V^{4+} distribution in the structure and the observed ^{31}P *ss*-NMR shifts, we generated four different input models for $Na_3V_2(PO_4)_2F_2O$ with four different terminal O-distributions. We assumed that the Na^+ ordering in this case was similar to the one used for $Na_3V_2(PO_4)_2F_3$. The structures of the input models are given in **Figure S5**. The as-mentioned models were relaxed until they reach their minimum energy. As no significant difference in the total energies (*E*) of all the calculated structural models were spotted, we conclude that they exhibit similar stability; hence, from DFT calculations, we do not predict any V^{3+} or V^{4+} ions segregation in the same bi-octahedron. The oxygen distribution on the terminal positions and hence the V^{3+}/V^{4+} distribution should be controlled solely by statistics leading to a random formation of V^{3+}–F–V^{3+}, V^{4+}–F–V^{4+} and V^{3+}–F–V^{4+} bi-octahedra. This aspect will be further discussed in the following part. Nevertheless, our different models allowed to compute the expected Fermi contact shifts for different V^{3+}/V^{4+} phosphorus local environments. In all models, the vanadium ions are found in the +3 state, with the same local electronic structure as in $Na_3V^{3+}{}_2(PO_4)_2F_3$, when localized in VO_4F_2 octahedral sites, whereas they are found in the +4 oxidation state, with the same local electronic structure as in $Na_3V^{4+}{}_2(PO_4)_2FO_2$, when localized in VO_5F octahedral sites. Therefore, one expects the same spin transfer mechanisms as those described above for V^{3+} in $Na_3V^{3+}{}_2(PO_4)_2F_3$ and V^{4+} in $Na_3V^{4+}{}_2(PO_4)_2FO_2$. As shown in **Figure 6** for model 1, where only the $P(OV^{3+})_2(OV^{4+})_2$ environment is detected, a spin transfer mechanism does occur only from the two V^{3+} ions leading to computed ^{31}P Fermi contact shifts in the range of 3282 - 3285 ppm (**Table 2**). 3D spin density maps of the other considered models can be found in the

supplementary information (**Figure S6**). In **Table 2**, we summarize the computed Fermi contact shifts depending on the phosphorus environments. DFT calculations thus allowed us to rationalize that in the $Na_3V_2(PO_4)_2F_3$ - $Na_3V_2(PO_4)_2FO_2$ solid solution, each V^{3+} ions located in the proximity of P contributes for ~1500 ppm to the Fermi contact shift whereas a V^{4+} ion does not lead to a significant shift. This confirms the signal assignment proposed earlier.[14]

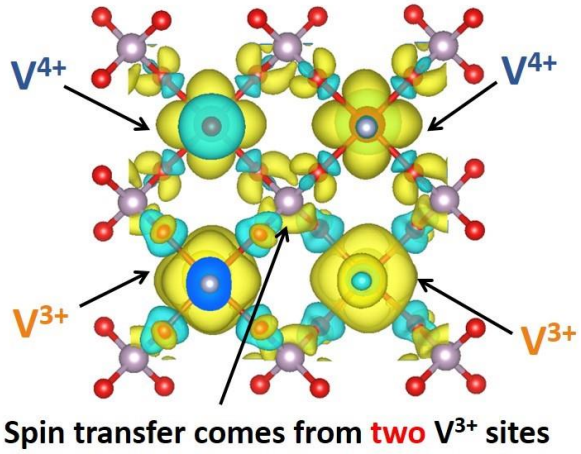

***Figure 6** : The spin distribution map showing $P(OV^{3+})_2(OV^{4+})_2$ local environment in Model 1 of $Na_3V_2(PO_4)_2F_2O$. The positive and negative electron spin are represented in yellow and blue, respectively.*

Table 2 : Phosphorus local environments generated from DFT calculations and their respective Fermi contact shifts in comparison to those observed experimentally.

	DFT calculations		**Experimental shift (ppm)**
	Local environment	Calculated shift (ppm)	
Model 3	$P(OV^{3+})_4$	5800 – 5900	6000
Model 2	$P(OV^{3+})_3(OV^{4+})$	4200 – 4600	4500
Model 1/ Model 4	$P(OV^{3+})_2(OV^{4+})_2$	3282 – 3285	3000
Model 2	$P(OV^{3+})(OV^{4+})_3$	1700 – 2100	1500
Model 3	$P(OV^{4+})_4$	665	~ 0

In order to further confirm the absence of spin transfer from V^{4+} ions to the phosphorus nuclei in the $Na_3V_2(PO_4)_2F_3$ - $Na_3V_2(PO_4)_2FO_2$ system, we chose to compare these results with those obtained for the partially aluminum-substituted composition $Na_3V_{1.5}Al_{0.5}(PO_4)_2F_3$, recently reported by our group.[32] Al^{3+} ions are diamagnetic, which are not able to cause any

Fermi contact with the neighboring P nuclei in the structure. In $Na_3V_{1.5}Al_{0.5}(PO_4)_2F_3$ composition, new phosphorus local environments are generated, *i.e.* $P(OV^{3+})_3(OAl^{3+})$, $P(OV^{3+})_2(OAl^{3+})_2$, $P(OV^{3+})(OAl^{3+})_3$ and $P(OAl^{3+})_4$, and they should exhibit similar shifts to those observed in $Na_3V^{3+}{}_{1.5}V^{4+}{}_{0.5}(PO_4)_2F_{2.5}O_{0.5}$. The ^{31}P *ss*-NMR spectrum of $Na_3V_{1.5}Al_{0.5}(PO_4)_2F_3$ is shown in **Figure 7** and indeed exhibits five different resonances at 6000 ppm, 4500 ppm, 3000 ppm, 1500 ppm, and 0 ppm, very similar to the spectra of the $Na_3V^{3+}{}_{1.6}V^{4+}{}_{0.4}(PO_4)_2F_{2.6}O_{0.4}$ composition. DFT calculations performed for the $Na_3V_{1.5}Al_{0.5}(PO_4)_2F_3$ composition further confirm that solely the V^{3+} ions contribute to the ^{31}P Fermi contact shifts for about 1500 ppm per V^{3+} through a delocalization mechanism (**Figure 7**).

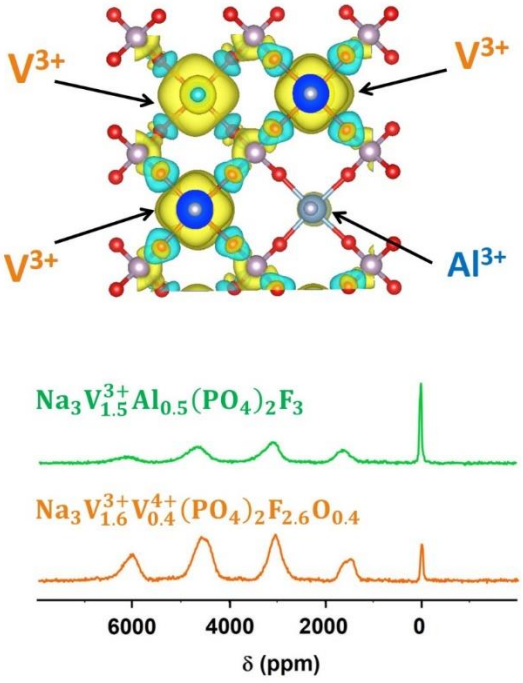

***Figure 7** : (Top) 3D calculated electronic spin map around P if one of the surrounding V^{3+} is substituted by Al^{3+}. (Bottom) ^{31}P MAS NMR spectra of $Na_3V_2(PO_4)_2F_{2.6}O_{0.4}$ and $Na_3V_{1.5}Al_{0.5}(PO_4)_2F_3$.*

^{23}Na *ss*-NMR Measurements in the $Na_3V_2(PO_4)_2F_3$ - $Na_3V_2(PO_4)_2FO_2$ solid solution

The ^{23}Na *ss*-NMR signatures of $Na_3V^{3+}_{2-y'}V^{4+}_{y'}(PO_4)_2F_{3-y'}O_{y'}$ ($0 \leq y' \leq 2$) phases have been studied in details by Park *et al* [26] who proposed that there were eight different paths to transfer the electron spin from the neighboring vanadium sites to Na^+; however, only two of them can give rise to a significant Fermi contact shift.[26] There are three different Na sites in the crystal structure of $Na_3V^{3+}_{2-y'}V^{4+}_{y'}(PO_4)_2F_{3-y'}O_{y'}$ phases [14,30] and the Na local environments of $Na_3V_2(PO_4)_2F_3$ ($y' = 0$) are described in **Figure S7**. Depending on the positions of the Na^+ ions in the channel, the spin diffusion paths can slightly vary; nevertheless, the two most dominant spin transfer mechanisms always come from the t_{2g} (V) – p_π (F1) – *s* (Na) orbital overlaps, with F1 as the sharing fluorine atom in the bi-octahedral units. The ^{23}Na *ss*-NMR Fermi contact shift depends on the number of V^{3+}/V^{4+} in its closest bi-octahedral unit.[26] In this previous study, the authors ignored the local distortion and the peculiar local electronic structure of the V^{4+} ions involved in a vanadyl bond. Actually, by considering the partial occupation of t_{2g} orbitals for V^{3+} ions (**Figure 2b** and **c)** and the d_{xz} occupation for V^{4+} ions as described previously (**Figure 3b** and **c**), the electronic spin transfer mechanism can be described differently. We here re-describe the spin transfer mechanism between V^{3+}/V^{4+} and the Na nuclei by considering the peculiar electronic structure of the V^{4+} ion. In $Na_3V^{3+}_2(PO_4)_2F_3$, among all the partially occupied t_{2g} orbitals, the d_{xz} one is properly oriented to form a π bond with F $2p_x$ that is pointing towards the 3*s* orbital of a nearby Na^+ in the channel, leading to a $3d_{xz}$ (V^{3+}) – $2p_x$ (F1) – 3*s* (Na) hybridized orbital suitable for the spin transfer through a delocalization mechanism (**Figure 8a**). As a result, a positive Fermi contact shift is observed for ^{23}Na. In $Na_3V^{4+}_2(PO_4)_2FO_2$, the single occupied orbital, $3d_{xy}$, of the V^{4+} ions (**Figure 3b** and **c**) cannot strongly overlap with the $2p_x$ orbital of F1 and the 3*s* orbital of Na (**Figure 8b**), resulting in a weaker Fermi contact shift. In $Na_3V_2(PO_4)_2F_{3-y'}O_{y'}$ oxygen-substituted phases, V^{3+} and V^{4+} co-exist in the structure and are distributed randomly over all the vanadium sites. This random distribution thus creates a third Na local environment, in which the Na nucleus resides next to

a bi-octahedron containing one V^{3+} and one V^{4+}. This Na nucleus is exposed to a strong interaction with V^{3+}, and to a weaker one with V^{4+}. The value of the ^{23}Na NMR shift in this case is expected to be lie between the values obtained in $Na_3V_2(PO_4)_2F_3$ and in $Na_3V_2(PO_4)_2FO_2$.

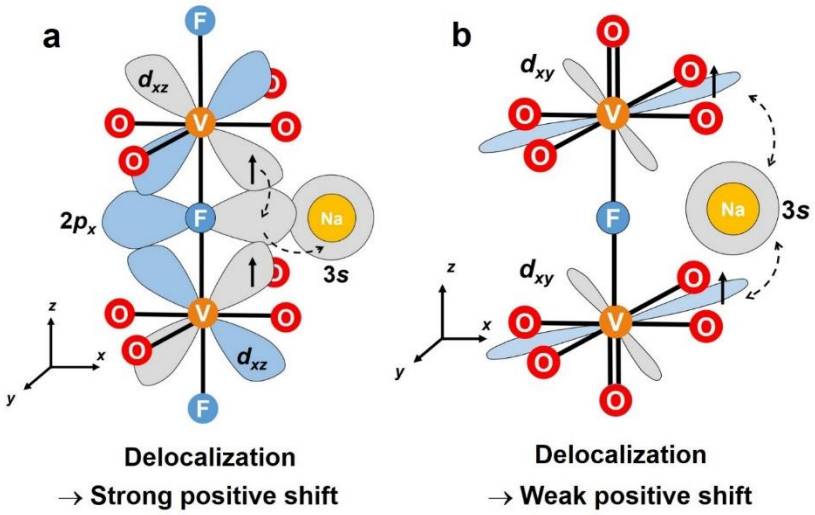

Figure 8 : *(a) The strong delocalization interaction between the electronic spin on orbital $3d_{xz}$ (V^{3+}) and Na nuclei in $Na_3V_2(PO_4)_2F_3$; (b) The weak delocalization interaction between the electronic spin on orbital $3d_{xy}$ (V^{4+}) and Na nuclei in $Na_3V_2(PO_4)_2FO_2$.*

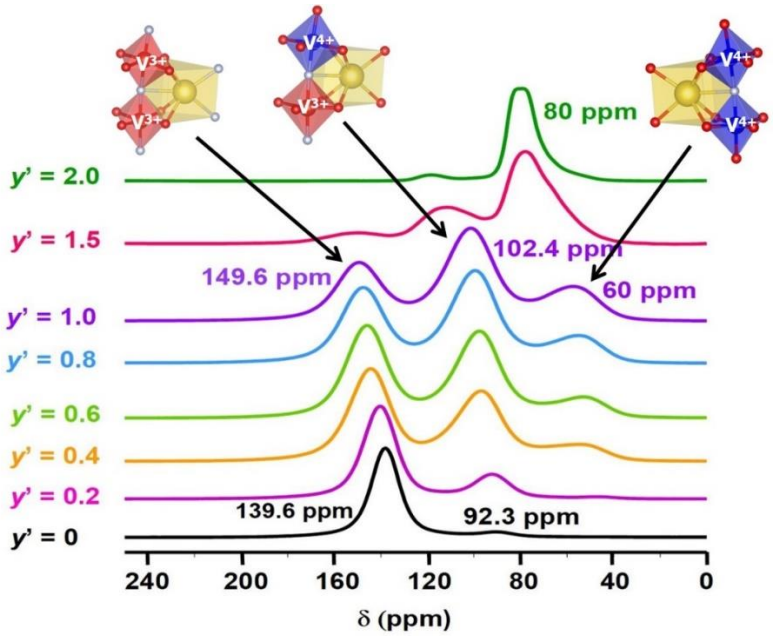

***Figure 9** : Selective single pulse ^{23}Na MAS NMR spectra of $Na_3V^{3+}_{2-y'}V^{4+}_{y'}(PO_4)_2F_{3-y'}O_{y'}$ ($0 \leq y' \leq 2$) samples (B_0 = 11.7 T; ν_R= 30 kHz). The Na sites are in yellow and $V^{3+}O_4F_2$ and $V^{4+}O_5F_1$ octahedral units in red and blue, respectively.*

Note that in our study, we had to consider different Na^+-Vacancy orderings or intermediate positions in order to model compounds with partial site occupancies. Therefore, the calculated Fermi contact shifts summarized in **Tables S3 and Table S4** do not reflect the exact positions observed experimentally for the ^{23}Na ss-NMR signals and will thus not be further discussed here. Nevertheless, our approach allows to confirm the signals assignment presented in **Figure 9**.

V^{3+}/V^{4+} distribution and the relative intensities of ^{23}Na and ^{31}P NMR resonances

As the ^{23}Na and ^{31}P NMR signals assignment was confirmed by our DFT calculations, one can analyze the relative intensities of the ^{31}P and ^{23}Na signals in order to discuss the local atomic and electronic structures of the series. If the V^{3+} and V^{4+} are distributed randomly over the whole structure, the probability of occurrence of each phosphorus or sodium local environment can be estimated using a binomial distribution:

$$C(n,k)p^k(1-p)^{(n-k)} = \left(\frac{n!}{k!\,(n-k)!}\right)p^k(1-p)^{(n-k)}$$

In the case of phosphorus, n = 4, i.e. the number of surrounding vanadium sites, k = 0, 1, 2, 3, or 4, *i.e*, the number of V^{4+} among the vanadium sites, and p is the percentage of V^{4+} for a given composition. For $Na_3V_2(PO_4)_2F_{3-y'}O_{y'}$ compositions, $p = y'/2$. In the case of sodium, n = 2 as the shift of each sodium is influenced by two neighboring vanadium sites, and k = 0, 1, or 2.

Figure 10a compares the experimental and theoretical relative intensities between the five ^{31}P *ss*-NMR resonances observed for $Na_3V_2(PO_4)_2F_2O$, characterized by half vanadium ions in the +4 state and half in the +3 state. The experimental values are in good agreement with those expected from binomial distribution supporting the assumption that F/O are distributed randomly in the whole structure.

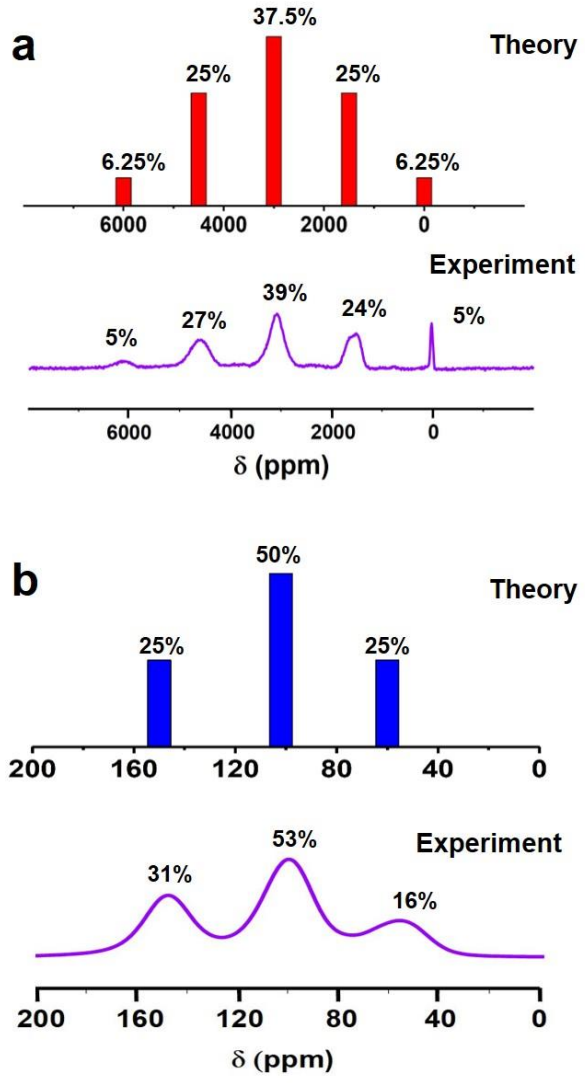

Figure 10 : Comparison betweeen theoretical and experimental relative intensities of (a) ^{31}P ss-NMR and (b) ^{23}Na ss-NMR resonances recorded on $Na_3V_2(PO_4)_2F_2O$.

In our previous publication, we stated that "the experimental intensities distribution does not follow the theoretical one if the repartition of V^{3+} and V^{4+} ions would have been statistical around each phosphorus: phosphorus nuclei appear to be experimentally surrounded by more V^{4+} than expected" [14]; in fact, the chemical formulas announced in [14] were not correct and we indeed had more V^{4+} than we had expected. With a correction of the chemical formula of these compounds in [31], the theoretical and experimental relative intensities determined for the ^{31}P NMR resonances of $Na_3V_2(PO_4)_2F_2O$ are in good agreement with each other. Note that the ^{31}P *ss*-NMR spectrum of $Na_3V_2(PO_4)_2F_2O$ is quite broad with resonances ranging from 0 ppm to 6000 ppm (**Figure 10a**), and depending on the position of the off-set of the excitation pulse, their relative intensities can vary significantly. This observation is demonstrated in **Figure S8**, where the off-set of the excitation was placed at 800 ppm, 2978 ppm, and 5000 ppm: the intensities of resonances close to the off-set are enhanced while those far away are underestimated. Furthermore, the resonances observed in $Na_3V_2(PO_4)_2F_2O$ have different relaxation times. When the refocalization delay of the echo acquisition is varied, the intensity of some peaks can be underestimated or overestimated (**Figure S9**). Therefore, the ^{31}P *ss*-NMR experimental measurements on $Na_3V_2(PO_4)_2F_2O$ are just semi-quantitative.

The theoretical relative intensities between ^{23}Na NMR resonances can also be calculated by the binomial equation considering a random distribution of V^{3+}/V^{4+} on two vanadium positions. The relative intensity of each ^{23}Na NMR signal can be extracted from the peak area calculated using the DM-fit software that uses different Pseudo-Voigt peak shape functions. All the observed ^{23}Na NMR resonances in the $Na_3V_2(PO_4)_2F_{3-y'}O_{y'}$ compositions can be fitted with a Pseudo-Voigt peak shape function, except the resonance at 80 ppm in $Na_3V_2(PO_4)_2FO_2$ composition which requires to be described by two peak functions. This could imply a Na ordering in the structure leading to two Na local environments which are slightly different from each other.[26] Nevertheless, the intensity of this resonance at 80 ppm was considered to be equal

to the sum of the area of these two signals. The theoretical and observed relative intensities between ^{23}Na NMR lines are given in **Figure 10b** as an example for the $Na_3V_2(PO_4)_2F_2O$ composition, the results for the other compositions being reported in **Table S5**.

The resonant region of the ^{23}Na *ss*-NMR signals is quite narrow; therefore, there is no influence of the off-set position on the relative intensities of the ^{23}Na *ss*-NMR signals, whose determination is thus quantitative. In this case, the binomial equation gives results which are in good agreement with the experimental ones proving that V^{3+}/V^{4+} are randomly distributed in these structures. Therefore, the relative intensities between ^{23}Na resonances can be used to estimate the *y*' value in a $Na_3V_2(PO_4)_2F_{3-y'}O_{y'}$ composition.

▪ CONCLUSIONS

The local atomic and electronic structures of the compositions belonging to the solid solution $Na_3V_2(PO_4)_2F_3$ – $Na_3V_2(PO_4)_2FO_2$ have been investigated by a combination of ^{23}Na and ^{31}P MAS NMR and DFT calculations. The experimental ^{31}P NMR Fermi contact shift values are in agreement with those calculated using the PAW approach implemented in the VASP code considering a Curie-Weiss law. The V^{3+} ions in $Na_3V_2(PO_4)_2F_3$ reside in a 'quasi'-symmetric octahedral site with its electron spins spreading out to the four neighboring phosphorus nuclei through the orbital overlap between its $3d_{xz}/3d_{yz}$ orbitals and the sp^3 hybridized orbital of phosphorus atoms via the O 2*p* orbital. Once oxygen substitution occurs, the vanadium ion bonded to this oxygen is oxidized to V^{4+} and form a vanadyl type bond with a very peculiar electronic structure: (d_{xy}^1). This highly covalent bond distorts the local structure of the vanadium ion, imposes further orbital splitting, and suppresses the spin transfer through $3d_{xz}$ and $3d_{yz}$ orbitals. A combination of these effects results in the formation of a $P(OV^{4+})_4$ environment with a shift in the diamagnetic ppm region. The ^{23}Na MAS NMR signals

assignment was also confirmed, and based on the relative intensity distribution of the signals properly assigned for both ^{31}P and ^{23}Na we conclude that no segregation of V^{4+} ions are observed in the $Na_3V_2(PO_4)_2F_3$ – $Na_3V_2(PO_4)_2FO_2$ electrode materials unlike what was suspected for the $LiVPO_4F$ – $LiVPO_4O$ series.[15]

▪ ASSOCIATED CONTENT

Supporting Information

Synchrotron XRD of $Na_3V_2(PO_4)_2F_{3-y'}O_{y'}$ ($0 \leq y' \leq 2$) (Figure S1); Experimental structure and the input model used in the DFT calculations for $Na_3V_2(PO_4)_2F_3$ (Figure S2); Experimental and optimized unit cell parameters of $Na_3V_2(PO_4)_2F_3$ calculated by GGA and GGA+U methods (Table S1); Experimental structure and the input model used in the DFT calculations for $Na_3V_2(PO_4)_2FO_2$ (Figure S3); Experimental and optimized unit cell parameters of $Na_3V_2(PO_4)_2FO_2$ calculated by GGA and GGA+U methods (Table S2); The splitting scheme of the five 3*d* orbitals of V^{3+} in $Na_3V_2(PO_4)_2F_3$ and those of V^{4+} in $Na_3V_2(PO_4)_2FO_2$ (Figure S4); Different optimized structures obtained for $Na_3V_2(PO_4)_2F_2O$ by DFT calculations (Figure S5); Different spin transfer pathways observed in $Na_3V_2(PO_4)_2F_2O$ by considering different V^{3+}:V^{4+} distributions (Figure S6); Na local environments in $Na_3V_2(PO_4)_2F_3$ (Figure S7); ^{23}Na NMR Fermi contact shifts calculated by GGA and GGA+U methods for $Na_3V_2(PO_4)_2F_3$ and $Na_3V_2(PO_4)_2FO_2$ (Table S3); ^{23}Na NMR Fermi contact shifts calculated by GGA method for $Na_3V_2(PO_4)_2F_2O$ (Table S4); ^{31}P *ss*-NMR spectra of $Na_3V_2(PO_4)_2F_2O$ recorded at different off-set positions (Figure S8); ^{31}P *ss*-NMR spectra of $Na_3V_2(PO_4)_2F_2O$ recorded at different refocalization delays (Figure S9). The Supporting Information is available free of charge on the ACS Publications website at DOI: .

AUTHOR INFORMATION

Corresponding Author:

*E-mail: Dany.Carlier@icmcb.cnrs.fr

Notes

The authors declare no competing financial interest.

ACKNOWLEDGEMENT

The authors acknowledge the French RS2E Network for the funding of LHBN's PhD thesis, the RS2E and Alistore-ERI networks for the funding of TB's postdoctoral fellowship, as well as the financial support of Région Nouvelle Aquitaine, of the French National Research Agency (STORE-EX Labex Project ANR-10-LABX-76-01 and SODIUM Descartes project ANR-13-DESC-0001-02) and of the European Union's Horizon 2020 research and innovation program under the Grant Agreement No. 646433-NAIADES. The Mésocentre de Calcul Intensif Aquitain (MCIA) and the modelling center of ISM are acknowledged for computing facilities. The authors want to thank Yohan BIECHER (ICMCB-CNRS) for his help with DMfit.

REFERENCES

(1) Armand, M.; Tarascon, J.-M. Building Better Batteries. *Nature* **2008**, *451* (7179), 652–657. (DOI: 10.1038/451652a).

(2) Tarascon, J.-M. and Armand, M. Issues and Challenges Facing Rechargeable Lithium Batteries. *Nature* **2001**, *414* (November), 359–367. (DOI: 10.1038/35104644)

(3) Goodenough, J. B.; Kim, Y. Challenges for Rechargeable Li Batteries. *Chem. Mater.* **2010**, *22*, 587–603. (DOI: 10.1021/cm901452z).

(4) Hwang, J.-Y.; Myung, S.-T.; Sun, Y.-K. Sodium-Ion Batteries: Present and Future. *Chem. Soc. Rev.* **2017**, *46* (12), 3529–3614. (DOI: 10.1039/C6CS00776G).

(5) Pell, A. J.; Pintacuda, G.; Grey, C. P. Progress in Nuclear Magnetic Resonance Spectroscopy Paramagnetic NMR in Solution and the Solid State. *Prog. Nucl. Magn. Reson. Spectrosc.* **2019**, *111*, 1–271. (DOI: 10.1016/j.pnmrs.2018.05.001).

(6) Murakami, M.; Noda, Y.; Koyama, Y.; Takegoshi, K.; Arai, H.; Uchimoto, Y.; Ogumi, Z. Local Structure and Spin State of Cobalt Ion at Defect in Lithium Overstoichiometric $LiCoO_2$ As Studied by $^{6/7}$Li Solid-State NMR Spectroscopy. *J. Phys. Chem. C* **2014**, *118* (28), 15375–15385. (DOI: 10.1021/jp5039909)

(7) Carlier, D.; Cheng, J.-H.; Pan, C.-J.; Ménétrier, M.; Delmas, C.; Hwang, B. DFT+U Calculations and XAS Study: Further Confirmation of the Presence of CoO_5 Square-Based Pyramids with IS-Co^{3+} in Li-Overstoichiometric $LiCoO_2$. *J. Phys. Chem. C* **2013**, *117* (50), 26493–26500. (DOI: 10.1021/jp409850q)

(8) Levasseur, S.; Ménétrier, M.; Shao-Horn, Y.; Gautier, L.; Audemer, A.; Demazeau, G.; Largeteau, A.; Delmas, C. Oxygen Vacancies and Intermediate Spin Trivalent Cobalt Ions in Lithium-Overstoichiometric $LiCoO_2$. *Chem. Mater.* **2003**, *15* (1), 348–354. (DOI: 10.1021/cm021279g)

(9) Ménétrier, M.; Shao-Horn, Y.; Wattiaux, A.; Fournès, L.; Delmas, C. Iron Substitution in Lithium-Overstoichiometric "$Li_{1.1}CoO_2$": Combined ^{57}Fe Mössbauer and ^{7}Li NMR Spectroscopies Studies. *Chem. Mater.* **2005**, *17* (18), 4653–4659. (DOI: 10.1021/cm0504384)

(10) Lee, Y. J.; Wang, F.; Grey, C. P. ^{6}Li and ^{7}Li MAS NMR Studies of Lithium Manganate Cathode Materials. *J. Am. Chem. Soc.* **1998**, *120* (48), 12601–12613. (DOI: 10.1021/ja9817794)

(11) Kim, J.; Middlemiss, D. S.; Chernova, N. A.; Zhu, B. Y. X.; Masquelier, C.; Grey, C. P. Linking Local Environments and Hyperfine Shifts: A Combined Experimental and Theoretical ^{31}P and ^{7}Li Solid-State NMR Study of Paramagnetic Fe(III) Phosphates. *J. Am. Chem. Soc.* **2010**, *132* (47), 16825–16840. (DOI: 10.1021/ja102678r)

(12) Li, Q.; Liu, Z.; Zheng, F.; Liu, R.; Lee, J.; Xu, G.; Zhong, G.; Hou, X.; Fu, R.; Chen, Z.; et al. Identifying the Structural Evolution of the Sodium Ion Battery Na_2FePO_4F Cathode. *Angew. Chemie Int. Ed.* **2018**, *57* (37), 11918–11923. (DOI: 10.1002/anie.201805555)

(13) Xu, J.; Lee, D. H.; Clément, R. J.; Yu, X.; Leskes, M.; Pell, A. J.; Pintacuda, G.; Yang, X.; Grey, C. P.; Meng, Y. S. Identifying the Critical Role of Li Substitution in P2–$Na_x[Li_yNi_zMn_{1-y-z}]O_2$ ($0 < x, y, z < 1$) Intercalation Cathode Materials for High-Energy

Na-Ion Batteries. *Chem. Mater.* **2014**, *26* (2), 1260–1269. (DOI: 10.1021/cm403855t)

(14) Broux, T.; Bamine, T.; Fauth, F.; Simonelli, L.; Olszewski, W.; Marini, C.; Ménétrier, M.; Carlier, D.; Masquelier, C.; Croguennec, L. Strong Impact of the Oxygen Content in $Na_3V_2(PO_4)_2F_{3-y}O_y$ ($0 \leq y \leq 0.5$) on Its Structural and Electrochemical Properties. *Chem. Mater.* **2016**, *28* (21), 7683–7692. (DOI: 10.1021/acs.chemmater.6b02659)

(15) Bamine, T.; Boivin, E.; Boucher, F.; Messinger, R. J.; Salager, E.; Deschamps, M.; Masquelier, C.; Croguennec, L.; Ménétrier, M.; Carlier, D. Understanding Local Defects in Li-Ion Battery Electrodes through Combined DFT/NMR Studies: Application to $LiVPO_4F$. *J. Phys. Chem. C* **2017**, *121* (6), 3219–3227. (DOI: 10.1021/acs.jpcc.6b11747)

(16) Boivin, E.; David, R.; Chotard, J.-N.; Bamine, T.; Iadecola, A.; Bourgeois, L.; Suard, E.; Fauth, F.; Carlier, D.; Masquelier, C.; et al. $LiVPO4F_{1-y}O_y$ Tavorite-Type Compositions : Influence of the Concentration of Vanadyl-Type Defects on the Structure and Electrochemical Performance. *Chem. Mater.* **2018**, *30*, 5682–5693. (DOI: 10.1021/acs.chemmater.8b02138)

(17) Boivin, E.; Chotard, J.-N.; Ménétrier, M.; Bourgeois, L.; Bamine, T.; Carlier, D.; Fauth, F.; Masquelier, C.; Croguennec, L. Oxidation under Air of Tavorite $LiVPO_4F$: Influence of Vanadyl-Type Defects on Its Electrochemical Properties. *J. Phys. Chem. C* **2016**, *120* (46), 26187–26198. (DOI: 10.1021/acs.jpcc.6b07342)

(18) Zhou, L.; Leskes, M.; Ilott, A. J.; Trease, N. M.; Grey, C. P. Paramagnetic Electrodes and Bulk Magnetic Susceptibility Effects in the in Situ NMR Studies of Batteries: Application to $Li_{1.08}Mn_{1.92}O_4$ Spinels. *J. Magn. Reson.* **2013**, *234*, 44–57. (DOI: 10.1016/j.jmr.2013.05.011)

(19) Shimoda, K.; Murakami, M.; Takamatsu, D.; Arai, H. Electrochimica Acta In Situ NMR Observation of the Lithium Extraction / Insertion From. *Electrochim. Acta* **2013**, *108*, 343–349. (DOI: 10.1016/j.electacta.2013.06.120)

(20) Pecher, O.; Bayley, P. M.; Liu, H.; Liu, Z.; Trease, N. M.; Grey, C. P. Automatic Tuning Matching Cycler (ATMC) in Situ NMR Spectroscopy as a Novel Approach for Real-Time Investigations of Li- and Na-Ion Batteries. *J. Magn. Reson.* **2016**, *265*, 200–209. (DOI: 10.1016/j.jmr.2016.02.008)

(21) Poli, F.; Kshetrimayum, J. S.; Monconduit, L.; Letellier, M. Electrochemistry Communications New Cell Design for In-Situ NMR Studies of Lithium-Ion Batteries. *Electrochem. commun.* **2011**, *13* (12), 1293–1295. (DOI: 10.1016/j.elecom.2011.07.019)

(22) Pecher, O.; Carretero-Gonzalez, J.; Griffith, K. J.; Grey, C. P. Materials' Methods: NMR in Battery Research. *Chem. Mater.* **2017**, *29* (1), 213–242. (DOI: 10.1021/acs.chemmater.6b03183)

(23) Ogata, K.; Salager, E.; Kerr, C. J.; Fraser, A. E.; Ducati, C.; Morris, A. J.; Hofmann, S.; Grey, C. P. Revealing Lithium-Silicide Phase Transformations in Nano-Structured Silicon-Based Lithium Ion Batteries via in Situ NMR Spectroscopy. *Nat. Commun.* **2014**, *5*, 1–11. (DOI: 10.1038/ncomms4217)

(24) Carlier, D.; Ménétrier, M.; Grey, C. P.; Delmas, C.; Ceder, G. Understanding the NMR Shifts in Paramagnetic Transition Metal Oxides Using Density Functional Theory Calculations. *Phys. Rev. B* **2003**, *67* (17), 174103(1)–174103(14). (DOI: 10.1103/PhysRevB.67.174103)

(25) Gover, R. K. B.; Bryan, A.; Burns, P.; Barker, J. The Electrochemical Insertion Properties of Sodium Vanadium Fluorophosphate, $Na_3V_2(PO_4)_2F_3$. *Solid State Ionics* **2006**, *177* (17–18), 1495–1500. (DOI: 10.1016/j.ssi.2006.07.028)

(26) Park, Y. U.; Seo, D. H.; Kim, H.; Kim, J.; Lee, S.; Kim, B.; Kang, K. A Family of High-Performance Cathode Materials for Na-Ion Batteries, $Na_3(VO_{1-x}PO_4)_2F_{1+2x}$ $(0 \leq x \leq 1)$: Combined First-Principles and Experimental Study. *Adv. Funct. Mater.* **2014**, *24* (29), 4603–4614. (DOI: 10.1002/adfm.201400561)

(27) Qi, Y.; Mu, L.; Zhao, J.; Hu, Y.; Liu, H.; Dai, S. Superior Na-Storage Performance of Low-Temperature-Synthesized $Na_3(VO_{1-x}PO_4)_2F_{1+2x}$ $(0 \leq x \leq 1)$ Nanoparticles for Na-Ion Batteries. *Angew. Chemie* **2015**, *127* (34), 10049–10054. (DOI: 10.1002/ange.201503188)

(28) Broux, T.; Fauth, F.; Hall, N.; Chatillon, Y.; Bianchini, M.; Bamine, T.; Leriche, J.; Suard, E.; Carlier, D.; Reynier, Y.; Simonin, L.; Masquelier, C.; Croguennec, L. High Rate Performance for Carbon-Coated $Na_3V_2(PO_4)_2F_3$ in Na-Ion Batteries. *Small Methods* **2019**, *3* (4), 1800215(1)–1800215(12). (DOI: 10.1002/smtd.201800215)

(29) Liu, Z.; Hu, Y.; Dunstan, M. T.; Huo, H.; Hao, X.; Zou, H.; Zhong, G.; Yang, Y.; Grey, C. P. Local Structure and Dynamics in the Na Ion Battery Positive Electrode Material $Na_3V_2(PO_4)_2F_3$. *Chem. Mater.* **2014**, *26* (8), 2513–2521. (DOI: 10.1021/cm403728w)

(30) Bianchini, M.; Brisset, N.; Fauth, F.; Weill, F.; Elkaim, E.; Suard, E.; Masquelier, C.; Croguennec, L. $Na_3V_2(PO_4)_2F_3$ Revisited: A High-Resolution Diffraction Study. *Chem. Mater.* **2014**, *26* (14), 4238–4247. (DOI: 10.1021/cm501644g)

(31) Nguyen, L. H. B.; Broux, T.; Camacho, P. S.; Denux, D.; Bourgeois, L.; Belin, S.; Iadecola, A.; Fauth, F.; Carlier, D.; Olchowka, J.; Masquelier, C.; Croguennec, L. Stability in Water and Electrochemical Properties of the $Na_3V_2(PO_4)_2F_3$ – $Na_3(VO)_2(PO_4)_2F$ Solid Solution. *Energy Storage Mater.* **2019**, *20*, 324–334. (DOI: 10.1016/j.ensm.2019.04.010)

(32) Olchowka, J.; Nguyen, L. H. B.; Broux, T.; Sanz Camacho, P.; Petit, E.; Fauth, F.; Dany, C.; Masquelier, C.; Croguennec, L. Aluminum Substitution for Vanadium in the $Na_3V_2(PO_4)_2F_3$ and $Na_3V_2(PO_4)_2FO_2$ Type Materials. *Chem. Commun.* **2019**, 55, 11719–11722. (DOI: 10.1039/C9CC05137F)

(33) Massiot, D.; Fayon, F.; Capron, M.; King, I.; Le Calvé, S.; Alonso, B.; Durand, J.; Bujoli, B.; Gan, Z.; Hoatson, G. Modelling One- and Two-Dimensional Solid-State NMR Spectra. *Magn. Reson. Chem.* **2002**, *40* (1), 70–76. (DOI: 10.1002/mrc.984)

(34) Kresse, G.; Furthmüller, J. Efficiency of Ab-Initio Total Energy Calculations for Metals and Semiconductors Using a Plane-Wave Basis Set. *Comput. Mater. Sci.* **1996**, *6* (1), 15–50. (DOI: 10.1016/0927-0256(96)00008-0)

(35) Shannon, R. D.; Prewitt, C. T. Effective Ionic Radii in Oxides and Fluorides. *Acta Crystallogr. Sect. B Struct. Crystallogr. Cryst. Chem.* **1969**, *25* (5), 925–946. (DOI: 10.1107/S0567740869003220)

(36) Momma, K.; Izumi, F. VESTA: A Three-Dimensional Visualization System for Electronic and Structural Analysis. *J. Appl. Crystallogr.* **2008**, *41* (3), 653–658. (DOI: 10.1107/S0021889808012016)

(37) Tsirlin, A. A.; Nath, R.; Abakumov, A. M.; Furukawa, Y.; Johnston, D. C.; Hemmida,

M.; Krug Von Nidda, H. A.; Loidl, A.; Geibel, C.; Rosner, H. Phase Separation and Frustrated Square Lattice Magnetism of $Na_{1.5}VOPO_4F_{0.5}$. *Phys. Rev. B - Condens. Matter Mater. Phys.* **2011**, *84* (1), 2–13. (DOI: 10.1103/PhysRevB.84.014429)

(38) Le Meins, J.-M.; Crosnier-Lopez, M.-P.; Hemon-Ribaud, A.; Courbion, G. Phase Transitions in the $Na_3M_2(PO_4)_2F_3$ Family (M = Al^{3+}, V^{3+}, Cr^{3+}, Fe^{3+}, Ga^{3+}): Synthesis, Thermal, Structural, and Magnetic Studies. *J. Solid State Chem.* **1999**, *148*, 260–277. (DOI: 10.1006/jssc.1999.8447)

(39) Castets, A.; Carlier, D.; Zhang, Y.; Boucher, F.; Marx, N.; Croguennec, L.; Ménétrier, M. Multinuclear NMR and DFT Calculations on the $LiFePO_4{\cdot}OH$ and $FePO_4{\cdot}H_2O$ Homeotypic Phases. *J. Phys. Chem. C* **2011**, *115* (32), 16234–16241. (DOI: 10.1021/jp204767c)

TOC

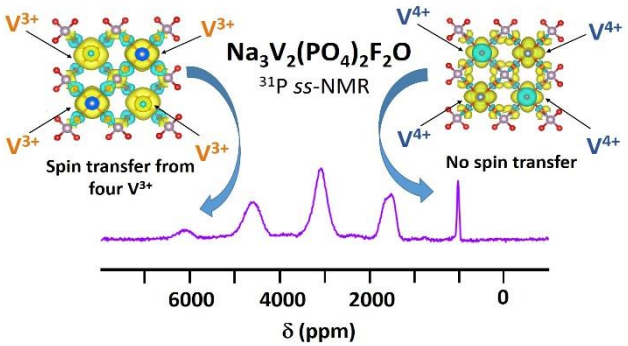
V3+
V3+
V3+
V3+
Na3V2(PO4)2F2O
31P ss-NMR
Spin transfer from
four V3+
V4+
V4+
V4+
V4+
No spin transfer
6000
4000
2000
0
δ (ppm)